Journal of Colloid and Interface Science 700 (2025) 138603

Contents lists available at ScienceDirect

Journal of Colloid And Interface Science

journal homepage: www.elsevier.com/locate/jcis

Ag-doping modulates the built-in electric field in S-scheme heterojunction of $ZnIn_2S_4$/covalent organic framework for efficient photocatalytic hydrogen peroxide production from pure water

Jiayi Meng, Yamei Huang, Yifan Liao, Quanmei Zhou, Yuchen Wei, Xinglin Wang, Linlin Gao, Wei-Lin Dai *

State Key Laboratory of Porous Materials for Separation and Conversion, Shanghai Key Laboratory of Molecular Catalysis and Innovative Materials, Department of Chemistry, Fudan University, Shanghai 200438, PR China

HIGHLIGHTS

- S-scheme heterojunction Ag-$ZnIn_2S_4$/TpBpy-COF photocatalyst was rationally constructed.
- High H_2O_2 yield of 4425 μmol·g^{-1}·h^{-1} from pure water, outperforming most reported photocatalysts.
- Ag doping adjusted the electronic and band structures of $ZnIn_2S_4$, forming S-scheme heterojunction.
- DFT confirmed robust electron transfer and efficient charge separation at the interface of the composite.

GRAPHICAL ABSTRACT

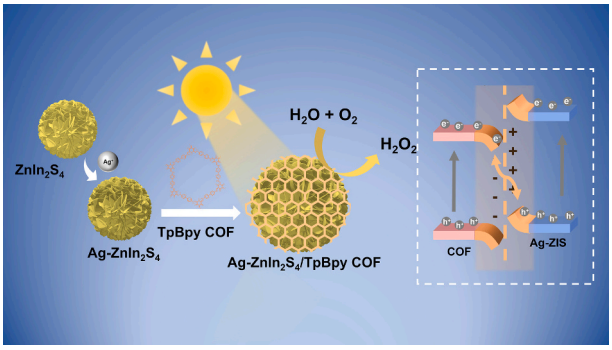

ARTICLE INFO

Keywords:
Ag-doping engineering
Charge transfer channel
Solar-to-H_2O_2 conversion
S-scheme heterojunction
Covalent organic frameworks

ABSTRACT

Covalent organic frameworks (COFs), characterized by efficient light absorption and highly tunable electronic structures, exhibit substantial promise for photocatalytic hydrogen peroxide (H_2O_2) production. To solve the problem of severe photogenerated carrier recombination, the researchers proposed to construct step-scheme (S-scheme) heterojunctions by combining COFs with metal sulfides (MS) to achieve effective separation and directional transfer of photogenerated electrons and holes. Herein, we deposited a bipyridine-linked COF (TpBpy) onto Ag-doped zinc indium sulfide (Ag-$ZnIn_2S_4$, denoted as Ag-ZIS) nanoflowers to construct an S-scheme heterojunction for photocatalytic H_2O_2 production. Employing room-temperature cation exchange engineering, atomic-level modulation of the ZIS lattice is achieved under mild conditions, inducing tunable bandgap narrowing and a red-shifted visible light absorption edge. Ag doping promotes the formation of S-scheme heterojunction and further optimizes the built-in electric field. The construction of the S-scheme heterojunction, which involves strong electronic coupling at the contact interface between Ag-ZIS and TpBpy COF, significantly reduces the recombination rate of photogenerated carriers, enhances charge transfer efficiency, and forms an efficient electron transfer channel. The optimized photocatalyst, Ag-ZIS/TpBpy COF-2 (denoted as AZC-2) exhibited excellent photocatalytic activity from pure water, with H_2O_2 yield reaching 4425 μmol·g^{-1}·h^{-1}. This

* Corresponding author.
E-mail address: wldai@fudan.edu.cn (W.-L. Dai).

https://doi.org/10.1016/j.jcis.2025.138603
Received 27 May 2025; Received in revised form 8 July 2025; Accepted 29 July 2025
Available online 31 July 2025

study highlights the great potential of ion doping strategies for advancing MS/COF-based S-scheme heterojunctions in solar-driven H_2O_2 synthesis.

1. Introduction

Hydrogen peroxide (H_2O_2), a crucial green oxidant, is widely used in pollutant treatment, environmental protection, and pharmaceutical synthesis due to its potent oxidizing capabilities and non-toxic nature [1–3]. However, the conventional anthraquinone process for H_2O_2 production is energy-intensive and requires high-temperature and high-pressure conditions, posing significant cost and safety challenges [4–6]. Photocatalytic synthesis of H_2O_2 has emerged as a promising green and non-polluting alternative [7,8]. Nevertheless, its efficiency remains limited by factors such as the light-absorbing capacity of photocatalysts, the separation and migration efficiency of photogenerated carriers, and the complexity of active sites [9].

To enhance the efficiency of photocatalytic H_2O_2 synthesis, various strategies have been investigated, among which doping engineering and heterojunction construction have proven particularly effective [10–12]. Doping can introduce electron traps or new transport channels to modulate the band structures of photocatalysts and expand their light absorption range [13]. Heterojunctions and composite structures formed by two or more different semiconductors, leverage interfacial electric field effects to facilitate the separation and migration of photogenerated carriers [14–17]. Through heterojunction construction, photogenerated electrons and holes can be spatially segregated and accumulated on distinct material surfaces, thereby enhancing photocatalytic reaction efficiency [18]. Among various heterojunction types, the step-scheme (S-scheme) heterojunction stands out for its ability to maintain strong redox capacity while spatially separating photogenerated electrons and holes, offering significant advantages in photocatalytic H_2O_2 production [19–22].

Zinc indium sulfide ($ZnIn_2S_4$), as a typical metal sulfide photocatalyst, has garnered considerable attention due to its unique electronic structure and tunable band structure [23–25]. However, the inefficient separation of photogenerated carriers limits the further improvement of its photocatalytic performance. A promising strategy to boost the photocatalytic efficiency of $ZnIn_2S_4$ (ZIS) involves modulating its band edge positions via the incorporation of foreign cations, especially distinct heterovalent ions [26,27]. Appropriate ion doping can enhance solar light utilization efficiency and modify the electronic and band structures of photocatalysts, thereby improving electrical conductivity and charge mobility. Crucially, the energy level structure directly influences the generation of active species during reactions, which is intrinsically linked to catalytic activity.

Covalent organic frameworks (COFs), unique metal-free polymeric porous materials, have received much focus due to their great crystallinity, large specific surface area, and tunable structural properties [28–30]. In 2020, Van Der Voort and colleagues [31] successfully developed the use of COFs as photocatalysts for H_2O_2 synthesis, opening up new possibilities for material design in photocatalytic H_2O_2 synthesis [32]. However, most COFs are primarily composed entirely of non-metallic elements, which restricts the number of catalytic active sites and results in relatively low catalytic performance. Constructing heterojunctions of COF with diverse nanomaterials, including metal sulfides (In_2S_3 [33,34], CdS [35]), metals (Au [36]), metal oxides (TiO_2 [37], WO_3 [38]), and metal-organic frameworks (MOFs [39]), has been shown to remarkably improve the efficiency of COFs in photocatalytic reactions.

Herein, we synthesized a series of Ag-doped ZIS (Ag-ZIS) via a facile room-temperature cation exchange strategy under mild reaction conditions and subsequently prepared Ag-ZIS/TpBpy COF (AZC) nanocomposites through a hydrothermal method. The synergistic effect of Ag doping and S-scheme heterojunction construction resulted in the remarkable photocatalytic activity of AZC for the synthesis of H_2O_2 from pure water, with an optimal rate of 4425 $\mu mol \cdot g^{-1} \cdot h^{-1}$, which surpasses most reported photocatalytic materials [15–17,40,41]. Combined experimental and theoretical analyses revealed that Ag doping not only optimized the electronic and band structure of ZIS but also facilitated the formation of an S-scheme heterojunction, both of which facilitate the efficient separation and transfer of carriers through a synergistic effect. This work presents a rational design strategy for photocatalysts that leverages the synergistic effect of ion doping and heterojunction construction to achieve efficient artificial photosynthesis. Moreover, it underscores the unique advantage of ion doping in modulating the built-in electric field within the metal sulfide/COF (MS/COF) S-scheme heterojunction.

2. Experimental

2.1. Materials

Zinc chloride ($ZnCl_2$, ≥98 %) was purchased from Sigma-Aldrich. Indium chloride tetrahydrate ($InCl_3 \cdot 4H_2O$, AR), thioacetamide (TAA, CH_3CSNH_2, AR), methanol, silver nitrate ($AgNO_3$, AR), acetone (AR) and dichloromethane (DCM, AR) were purchased from Sinopharm Chemical Reagent Co., Ltd. Polyvinylpyrrolidone (PVP) (Mw = 10,000), *N*,*N*-dimethylacetamide (DMAC, ≥99.8 %), 5,5′-diamine-2,2′ -bipyridine (Bpy, ≥97 %) were purchased from Aladdin Bio-Chem Technology Co., Ltd. The *o*-dichlorobenzene (*o*-DCB, 98 %), acetic acid (AcOH, 36 %) and 1,3,5-triformylphloroglucinol (Tp, 99.6 %) were purchased from Shanghai Maclin Biochemical Technology Co., Ltd. Tri-n-butylphosphine (TBP, 95 %) was purchased from Energy Chemical. Deionized (DI) water and ethanol (C_2H_5OH, AR) were used as received without further purification.

2.2. Synthesis of ZIS

A simple hydrothermal method was used to prepare ZIS samples. $ZnCl_2$ (0.4 mmol) and $InCl_3 \cdot 4H_2O$ (0.8 mmol) were first added to 30 mL of deionized water and stirred for 10 min. An excess of thioacetamide (TAA, 3.2 mmol) was added to the mixed solution and stirring was continued for 30 min. Afterwards, the resulting mixture was transferred to a Teflon-lined stainless-steel autoclave with a volume of 50 mL. The autoclave was sealed and kept under hydrothermal conditions at 180 °C for 24 h. The autoclave was then cooled to room temperature. After cooling naturally to room temperature, the samples were washed three times by centrifugation with deionized water and ethanol, respectively. Finally, the washed samples were dried in a vacuum oven at 60 °C overnight.

2.3. Synthesis of Ag-ZIS

Polyvinylpyrrolidone (PVP) solution was prepared by dissolving 0.2 g of PVP (Mw = 10,000) in a mixture of 10 mL of deionized water and 10 mL of methanol. 50 mg of the as-prepared ZIS powder was added to the PVP solution and stirred vigorously for 60 min. 30 μL of soft base tri-n-butylphosphine (TBP) was added to slow down the exchange kinetics and stirring was continued for 10 min. During stirring, an amount of 1 mM $AgNO_3$ aqueous solution was gradually added dropwisely. The mixture was stirred for 60 min under normal conditions. Then the resulting sample was washed three times by centrifugation with deionized water and ethanol. Finally, the washed samples were dried in vacuum at 60 °C overnight. The resulting composites were synthesized with 1, 2.5, 5 and 7.5 mL of aqueous $AgNO_3$ solution.

2.4. Synthesis of TpBpy COF

Synthesis of TpBpy COF was achieved solvothermally by reacting 1,3,5-triformylphloroglucinol (Tp) (0.3 mmol) and 2,2′-bipyridine-5,5′-diamine (Bpy) (0.45 mmol) using the *N*,*N*-dimethylacetamide (4.5 mL) and *o*-dichlorobenzene (1.5 mL) solvent mixture with acetic acid (0.6 mL, 6 M). The mixture was homogenously dispersed by ultrasonication for 15 min and degassed through three successive freeze-pump-thaw cycles. Then the tube was vacuum sealed and heated in an isothermal oven at 120 °C for 72 h. Finally, the product was filtered out and washed with excess DMAC, acetone, and dichloromethane. The as-obtained material was dried under vacuum at 150 °C for 24 h to obtain the as-synthesized TpBpy COF.

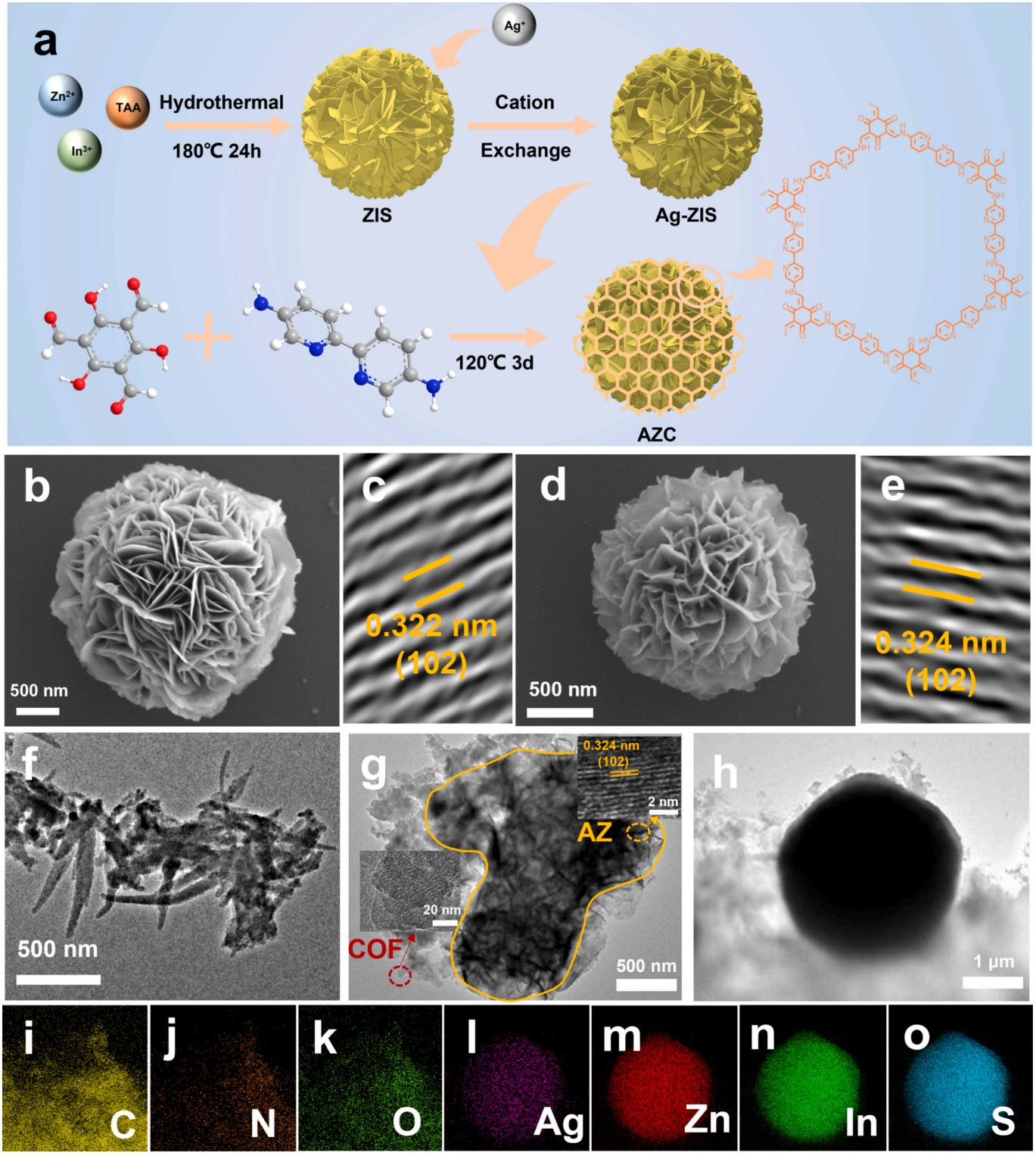

Fig. 1. (a) Synthesis route of the Ag-ZIS and AZC. SEM of (b) ZIS and (d) Ag-ZIS. HRTEM of (c) ZIS and (e) Ag-ZIS. TEM of (f) TpBpy COF and (g,h) AZC-2. (i-o) EDX elemental mappings of C, N, O, Ag, Zn, In, and S in AZC-2.

2.5. Synthesis of AZC and ZIS/TpBpy COF (ZC)

AZC composites were synthesized by an in situ solvothermal method. The general procedure was the same as that described above for TpBpy COF synthesis. Pre-prepared AZ powder (20 mg) was added to the mixture before ultrasonic treatment. The resulting sample was named as AZC-2. For comparison, the different weights of the composites were named as AZC-x (x = 1, 2, 3). The ZC composites were prepared by replacing AZ with ZIS in the above steps.

3. Results and discussion

3.1. Materials synthesis and characterization

The synthesis process of the photocatalyst is illustrated in Fig. 1a. Initially, nanoflower-like ZIS composed of nanosheets was successfully synthesized via a hydrothermal method. Subsequently, Ag-ZIS was prepared through a room-temperature cation exchange method. Finally, TpBpy COF was encapsulated onto the surface of Ag-ZIS using an in situ growth method to form the AZC composites. The microscopic morphology of the prepared samples was characterized using scanning electron microscopy (SEM), transmission electron microscopy (TEM), and high-resolution transmission electron microscopy (HRTEM). Both ZIS and Ag-ZIS exhibited similar nanoflower morphologies composed of nanosheets (Fig. 1b, d; Fig. S1a–b), indicating that ion doping does not significantly affect the overall morphology. TpBpy COF displayed an elongated, entangled nanowire morphology (Fig. 1f; Fig. S2). HRTEM images revealed a crystal lattice spacing of 0.322 nm for ZIS and 0.324 nm for Ag-ZIS, corresponding to the (102) crystal plane (Fig. 1c, e). The change in lattice spacing confirms the effective doping of Ag into the ZIS lattice and suggests slight lattice expansion due to the larger ionic radius of Ag compared to the replaced ions. In the TEM images of AZC-2, the darker region within the yellow boundary corresponds to Ag-ZIS, whereas the lighter region around it corresponds to TpBpy COF (Fig. 1g–h), confirming the effective encapsulation of COF onto the Ag-ZIS surface. Furthermore, Energy dispersive X-ray (EDX) elemental mapping results (Fig. 1i–o and Fig. S3) confirmed the uniform distribution of C, N, O, Ag, Zn, In, and S elements throughout AZC-2.

The crystal structures of the prepared samples were characterized using powder X-ray diffraction (PXRD). In Fig. 2a, the diffraction peaks at 21.3°, 27.7°, and 47.4° correspond to the (006), (102), and (110) crystal planes of ZIS, respectively, demonstrating the successful synthesis of ZIS. The diffraction patterns of the Ag-doped samples closely resemble those of the undoped ZIS, demonstrating that Ag doping does not alter the overall crystalline phase structure of ZIS. Notably, a slight shift in the (110) diffraction peak of 1.6 % Ag-ZIS was observed, moving from 47.4° to 47.0° (Fig. 2b), which suggests lattice expansion due to the substitution of larger Ag ions into the ZIS lattice. This observation is

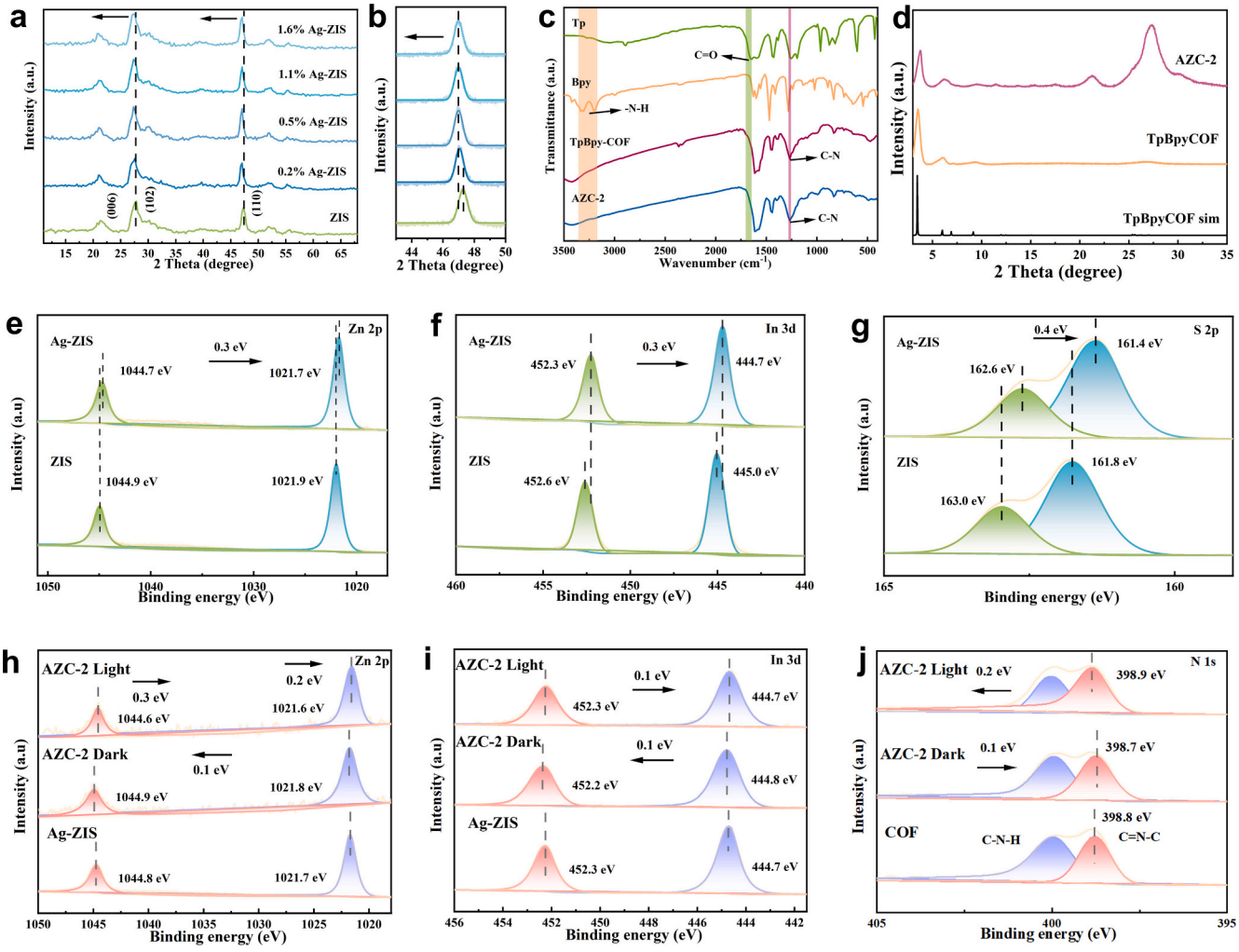

Fig. 2. (a) XRD pattern of different samples. (b) Partially enlarged view of (a). (c) FT-IR spectra of Tp, Bpy, TpBpy COF, and AZC-2. (d) PXRD pattern of AZC-2, simulated and experimental TpBpy COF. High-resolution XPS spectrum of (e) Zn 2p, (f) In 3d, and (g) S 2p for ZIS and Ag-ZIS. ISI-XPS of Zn 2p (h), In 3d (i) and N 1 s (j) for Ag-ZIS and AZC-2.

consistent with the increased lattice spacing detected in the HRTEM images of Ag-ZIS compared to ZIS (Fig. 1c, e). To further investigate elemental composition variations, X-ray photoelectron spectroscopy (XPS) and inductively coupled plasma optical emission spectrometry (ICP-OES) analyses were conducted. While ICP-OES probes the bulk elemental composition, XPS provides information on the surface composition. As detailed in Table S1, the Zn/In elemental ratios determined by XPS and ICP-OES were 0.468 and 0.484, respectively, for the pristine ZIS sample. Upon Ag ion doping, the Zn/In ratio on the sample surface, as determined by XPS, decreased to 0.392. In contrast, ICP-OES analysis revealed no significant change in the Zn/In ratio. This discrepancy suggests that Ag ions primarily substitute for Zn in ZIS at the surface level. The overall Zn (at.%)/In (at.%) ratio remains relatively stable, indicating that the extent of Ag substitution is limited and does not significantly affect the bulk composition of the material. Fourier-transform infrared (FT-IR) spectroscopy was employed to confirm the successful formation of the samples (Fig. 2c). The spectrum of Tp exhibited a characteristic peak at 1651 cm^{-1}, attributed to the C═O stretching vibration, while the broad absorption band spanning from 3150 cm^{-1} to 3400 cm^{-1} was assigned to the amino group in Bpy. For both COF and AZC-2, the C═O and -NH_2 peaks disappeared, and a new peak emerged at 1266 cm^{-1}, indicative of C—N bond formation, thereby confirming the successful synthesis of TpBpy COF. The FT-IR spectrum of AZC-2 closely resembled that of TpBpy COF, suggesting that the composite formation process did not compromise the structural integrity of the COF. The PXRD pattern of TpBpy COF displayed peaks at $2\theta = 3.5^{\circ}$ (100) and 26.0° (002), corresponding to the open-channel structure and interlayer π-π stacking, respectively (Fig. 2d). The close alignment between experimental and simulated PXRD patterns further supports the high crystallinity of the synthesized TpBpy COF. Additionally, various AZC compositions exhibited characteristic diffraction peaks of both TpBpy COF and Ag-ZIS (Fig. S4). The absence of significant peak shifts or new peaks in AZC emphasizes the preservation of the original lattice structures, indicating that the component integration maintained the crystallographic integrity of each phase. Nitrogen adsorption-desorption experiments were conducted to analyze the porous structure and specific surface area of the samples. Ag-ZIS displayed a classic type-IV isotherm with H3 type hysteresis loops, indicative of a mesoporous structure (Fig. S5). In contrast, TpBpy COF displayed a distinctive type-IV isotherm, confirming its mesoporous nature (Fig. S6). AZC-2 also showed a type-IV isotherm (Fig. S7), suggesting the retention of mesoporous characteristics. The specific surface areas calculated via Brunauer-Emmett-Teller (S_{BET}) analysis were 89.6 $m^2 \cdot g^{-1}$ for Ag-ZIS, 408.0 $m^2 \cdot g^{-1}$ for COF, and 361.4 $m^2 \cdot g^{-1}$ for AZC-2 (Table S2). The average pore diameters (D_{pore}) were 6.3 nm for Ag-ZIS, 4.6 nm for COF, and 5.3 nm for AZC-2. The introduction of Ag-ZIS into the COF filled part of the mesopores on the COF surface, resulting in a decrease in S_{BET} and D_{pore}. The intermediate S_{BET} of AZC-2 between Ag-ZIS and COF implies the formation of a tight interfacial heterostructure between Ag-ZIS and COF, thereby fine-tuning the material's surface properties. In addition, Ag-ZIS and COF have similar mesoporous structures, which are conducive to the adsorption and transport of reactants during the photocatalytic process.

XPS was employed to investigate the surface chemical composition and electronic structure. The XPS survey spectra (Fig. S8) confirmed the presence of Zn, In, and S in ZIS, with the additional presence of Ag in Ag-ZIS. The high-resolution XPS spectrum of Zn 2p for ZIS (Fig. 2e) exhibited two distinct peaks at 1021.9 eV and 1044.9 eV, assigned to Zn^{2+} $2p_{3/2}$ and Zn^{2+} $2p_{1/2}$. Similarly, the In 3d spectrum (Fig. 2f) exhibited peaks at 445.0 eV and 452.6 eV, attributed to In^{3+} $3d_{5/2}$ and In^{3+} $3d_{3/2}$. In the S 2p XPS spectrum of ZIS (Fig. 2g), two characteristic peaks at 161.8 eV and 163.0 eV were identified as the S^{2-} $2p_{3/2}$ and S^{2-} $2p_{1/2}$ spin-orbit components. After Ag ion doping, the binding energies of Zn 2p, In 3d, and S 2p in Ag-ZIS shifted downward by 0.3 eV, 0.3 eV, and 0.4 eV, respectively, compared to the pristine ZIS. These shifts indicate that Ag ion introduction modulates the electronic structure of ZIS, altering the binding energies of its constituent elements. In situ light irradiated X-ray photoelectron spectroscopy (ISI-XPS) (Fig. 2h–j, Fig. S9–S11) was used to analyze the electron migration direction in the heterojunction before and after illumination. Upon compounding Ag-ZIS and COF, Zn and In in Ag-ZIS shifted 0.1 eV to higher binding energies, while N in COF shifted to a lower binding energy. This finding suggests electron transfer from Ag-ZIS to COF at the heterojunction interface. After illumination, the binding energies of Zn and In in Ag-ZIS shifted to lower values, whereas that of N increased. This result implies that photogenerated electrons from COF in AZC-2 transfer to Ag-ZIS upon illumination, providing compelling evidence for the existence of an S-scheme heterojunction. To visualize the electron transport pathway, Au nanoparticles were introduced into the photocatalytic system as electron tracers through a photochemical deposition process. According to the TEM and EDX elemental mapping results, Au nanoparticles were found to selectively deposit on the Ag-ZIS component, rather than on the TpBpy COF. Notably, the spatial distribution of these nanoparticles shows a high degree of consistency with the variation trends observed in the ISI-XPS binding energy shifts. These findings provide strong evidence supporting the formation of an S-scheme heterojunction, with efficient charge separation following the characteristic S-scheme mechanism (Fig. S12).

3.2. Optical and electrochemical properties

To reveal the intrinsic role of heterovalent ion doping and the formation of organic-inorganic heterojunctions in enhancing photocatalytic performance in this system, we systematically investigated the photoelectronic properties of ZIS, Ag-ZIS, COF, and AZC. Optical absorption properties and band structures of the materials were characterized through ultraviolet-visible diffuse reflectance spectroscopy (UV–Vis DRS) combined with Mott-Schottky (M-S) analysis. The UV–Vis DRS spectrum of pure ZIS showed weak light absorption in the visible range (Fig. 3a). Notably, a red-shifted absorption edge was observed in Ag-ZIS compared to pristine ZIS, which suggests improved light absorption and expanded solar spectrum utilization. This red-shift may occur because the ion doping introduces defective states in the ZIS lattice, which alters the light absorption properties of the material to absorb light at longer wavelengths. Despite this improvement, light absorption of Ag-ZIS remains relatively weak compared to COF, which demonstrates strong visible light absorption. The optical absorption of AZC composites significantly increased with rising COF content, attributed to COF's superior light-harvesting properties. Bandgap energies (E_g) determined by Tauc plots were 2.56 eV for ZIS, 2.45 eV for Ag-ZIS, and 2.11 eV for COF (Fig. 3b), illustrating that Ag incorporation narrows the bandgap. Mott-Schottky plots (Fig. 3c-e) revealed positive slopes for ZIS, Ag-ZIS, and COF, confirming their n-type semiconductor nature. Their flat band potentials (E_{fb}) versus the saturated calomel electrode (SCE) are −0.56 V, −0.78 V, and − 0.39 V, respectively, and thus correspond to −0.76 V, −0.98 V, and − 0.59 V relative to the standard hydrogen electrode (NHE) ($E_{NHE} = E_{SCE} + 0.2$ V). According to semiconductor physics theory, the E_{fb} is approximately equivalent to the Fermi level (E_F), and the conduction band potential (E_{CB}) minimum is typically 0.2 V more negative than E_F. Based on this, the E_{CB} of ZIS, Ag-ZIS, and COF are calculated to be −0.56 V, −0.78 V, and − 0.39 V (vs NHE) (Fig. S13). Ag-ZIS displayed a stronger photocurrent response than pure ZIS (Fig. 3f), primarily attributed to ion doping modifying the band structure and electronic properties, enhancing photogenerated carrier mobility, and reducing electron-hole recombination. Forming a heterojunction with COF further amplified the photocurrent, improving carrier separation and transport. Ag-ZIS showed a smaller Nyquist plot radius in electrochemical impedance spectroscopy (EIS) compared to pure ZIS, and the radius decreased further upon COF incorporation, signifying reduced charge transfer resistance and superior charge transport in AZC (Fig. 3g). Photoluminescence (PL) spectra of TpBpy COF under 300 nm excitation featured a strong peak at 630 nm (Fig. 3h),

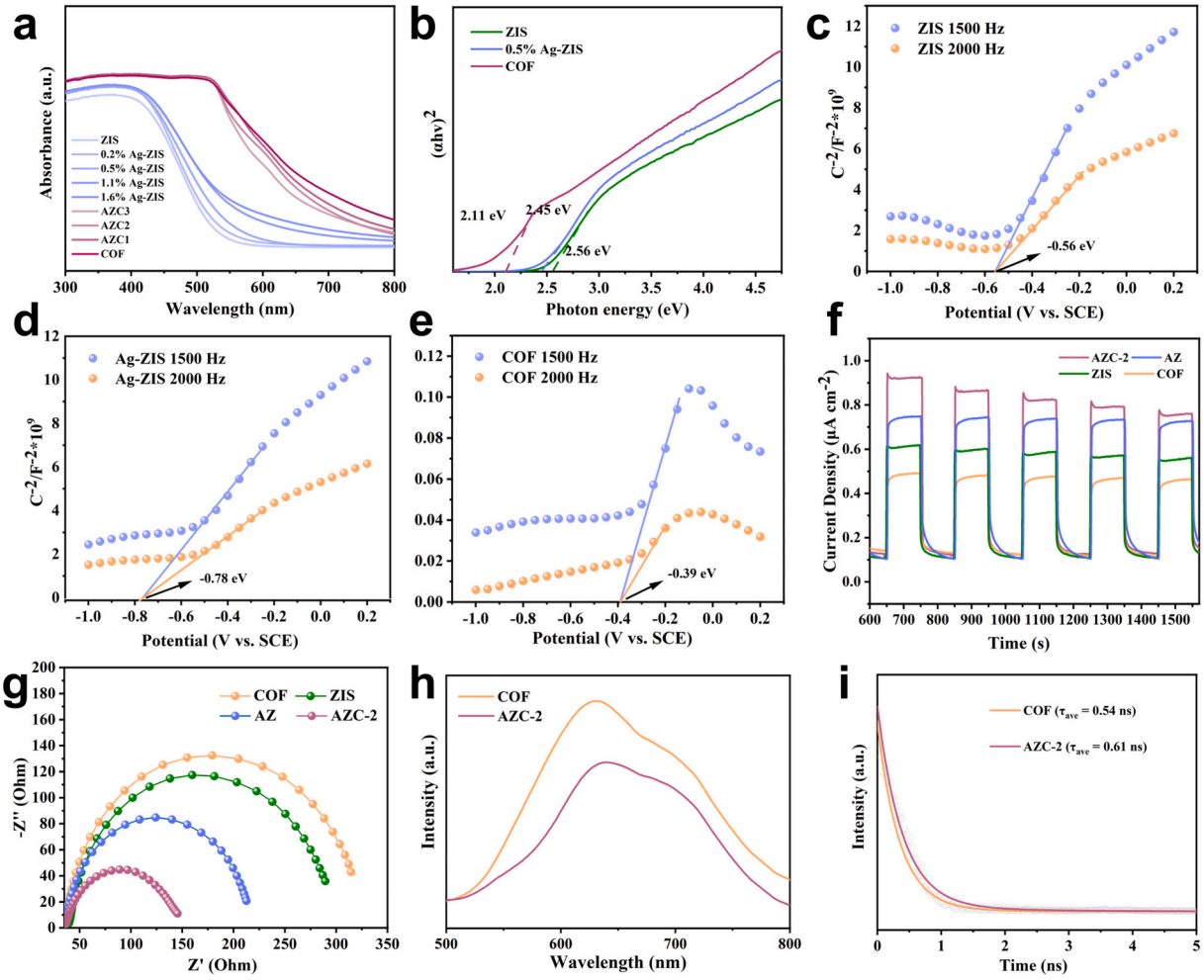

Fig. 3. (a) UV–Vis DRS spectra (b) and Tauc plots of the prepared materials. (c) M-S plots of ZIS, (d) Ag-ZIS (e) and COF. (f) Transient photocurrent responses. (g) EIS Nyquist plots. (h) PL spectra of COF and AZC-2. (i) Time-resolved PL spectra of COF and AZC-2.

which was markedly quenched in AZC-2, evidencing effective suppression of photogenerated carrier recombination. Besides, the charge separation kinetics of photocarriers were probed via time-resolved photoluminescence (TRPL) spectroscopy (Fig. 3i). The average fluorescence decay lifetime of AZC-2 (0.61 ns) is longer than that of TpBpy COF (0.54 ns), suggesting more efficient separation and transfer of photogenerated carriers in AZC-2 compared to TpBpy COF, in agreement with the above characterization results.

3.3. Photocatalytic H_2O_2 production performance

The photocatalytic hydrogen peroxide synthesis performance of the samples was evaluated under visible light (λ>420 nm) from pure water. In Fig. 4a and Fig. S14, the pristine ZIS exhibited inefficient photocatalytic H_2O_2 activity (102 μmol·g^{-1}·h^{-1}). After introducing Ag ions into the ZIS, the H_2O_2 yields of all Ag-ZIS samples with different doping amounts were significantly increased. Among these, 0.5 % Ag-ZIS achieved the highest photocatalytic H_2O_2 yield of 586 μmol·g^{-1}·h^{-1}, approximately 5.7 times higher than pristine ZIS. However, further increasing the Ag doping amount led to a decline in photocatalytic performance, likely due to the agglomeration of excess Ag ions, which hinders the transfer of photogenerated carriers. In contrast, the AZC composites demonstrated outstanding photocatalytic activity compared to the single components, with AZC-2 achieving the highest activity of 4425 μmol·g^{-1}·h^{-1} (Fig. 4b, Fig. S15). Notably, the photocatalytic yield of the composite without Ag ion doping (ZC-2) was significantly lower than that of AZC-2, highlighting the significant impact of Ag ion introduction on catalytic activity. Photocatalytic H_2O_2 production depends on both the generation and decomposition rates of H_2O_2. In the decomposition experiment (Fig. S16), pristine ZIS and AZ showed minimal degradation of the initially added H_2O_2, whereas AZC-2 not only avoided degradation but also generated additional H_2O_2, even exceeding the amount generated by TpBpy COF. This finding indicates that the AZC composites effectively promote H_2O_2 production even at higher initial H_2O_2 concentrations. Furthermore, AZC-2 exhibited superior catalytic stability, maintaining consistent catalytic activity over four consecutive cycles (Fig. 4c). XRD and FT-IR before and after the cycling of AZC-2 composite material demonstrated that the chemical state, crystal structure, and morphology of AZC-2 remained unchanged after the cycling (Fig. S17–18). Fig. 4d illustrates that the apparent quantum yield (AQY) curve is consistent with the UV–Vis DRS spectra, indicating that the reaction is indeed a light-driven redox process. The maximum AQY was 3.66 % at 450 nm, suggesting that AZC-2 can effectively utilize visible light, which is essential for enhancing its photoactivity. Overall, AZC-2 demonstrates exceptional photocatalytic H_2O_2 performance, surpassing many previously reported COF-based and MS-based photocatalysts (Fig. 4e, Table S3).

3.4. Photocatalytic mechanism and theoretical calculation

According to the current research findings, photocatalytic synthesis of hydrogen peroxide encompasses a series of intricate, continuous re-

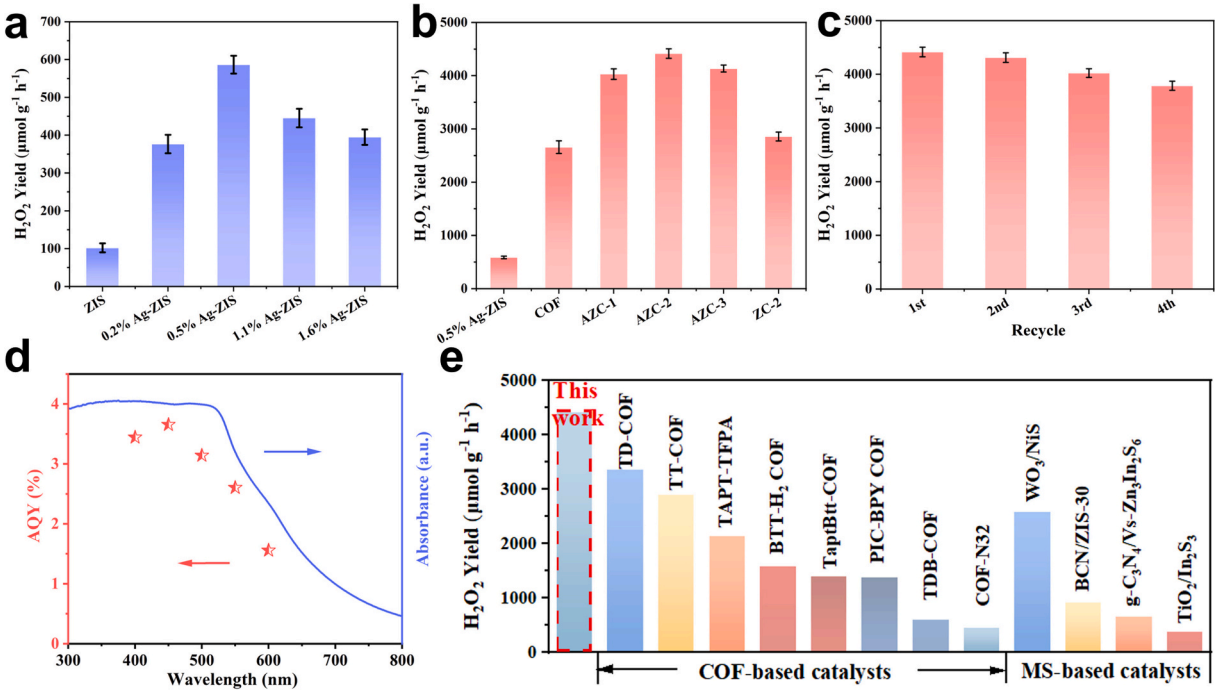

Fig. 4. (a,b) Photocatalytic production of H_2O_2 (three replicates) over comparative samples under 1 h of light irradiation. (c) Cycling stability (three replicates) of AZC-2. (d) AQY of AZC-2. (e) Photocatalytic H_2O_2 production rate of different reported photocatalysts [15,16,21,40–46].

actions that can be categorized into two primary components: the oxygen reduction reaction (ORR) and the water oxidation reaction (WOR). During the ORR, oxygen molecules adsorbed on the catalyst surface undergo a two-electron reduction process. This involves the initial formation of superoxide radicals ($\cdot O_2^-$) through the transfer of one electron to O_2, followed by the subsequent protonation and addition of a second electron to yield H_2O_2. The mechanism can be represented as follows:

$$O_2 + e^- \rightarrow \cdot O_2^- \quad (1)$$

$$\cdot O_2^- + 2H^+ + e^- \rightarrow H_2O_2 \quad (2)$$

Simultaneously, the WOR proceeds through the oxidation of water molecules. Here, photogenerated holes play a crucial role in oxidizing water to produce hydroxyl radicals (·OH) and oxygen:

$$H_2O + h^+ \rightarrow \cdot OH + H^+ \quad (3)$$

$$\cdot OH + \cdot OH \rightarrow H_2O_2 \quad (4)$$

$$2H_2O + 4h^+ \rightarrow O_2 + 4H^+ \quad (5)$$

The overall photocatalytic H_2O_2 production process is a synergistic interplay between these two reaction pathways. Optimizing charge carrier dynamics plays a vital role in suppressing electron-hole pair recombination, thus significantly enhancing the formation efficiency of reactive oxygen species (ROS) such as $\cdot O_2^-$ and ·OH. These ROS are pivotal intermediates in the synthesis of H_2O_2. Rational engineering of photocatalysts with precisely tailored band structures and active sites can effectively promote both ORR and WOR pathways, improving the overall efficiency of hydrogen peroxide production. By optimizing the electronic structure and surface properties of the photocatalyst, it is possible to achieve a higher selectivity and activity for the two-electron ORR pathway.

To explore the reaction pathways, free radical inhibition experiments, in situ FTIR analysis, and electron paramagnetic resonance (EPR) analysis were employed. As shown in Fig. 5a, we investigated the effects of different scavengers and various conditions on the capability of AZC-2 to produce H_2O_2. The extremely low yield of AZC-2 in the dark condition indicates the importance of light for photocatalytic H_2O_2 production. In an Ar atmosphere, almost no H_2O_2 was produced, proving that the process in AZC-2 photocatalysis is an ORR process with oxygen as the reactant. Besides, compared to the pure water system, the concentration of H_2O_2 in the BQ and $AgNO_3$ solutions was significantly lower, suggesting that $\cdot O_2^-$ and e^- are the dominant active species contributing to the photocatalytic H_2O_2 synthesis by AZC-2. To visualize the reaction pathways, in-situ FT-IR analysis was performed. In Fig. 5b, the intermediate signals were progressively strengthened with increasing illumination time. The peak at 1178 cm^{-1} in the spectrum belongs to $*O_2^-$, and the peak at 1380 cm^{-1} is assigned to the progressively generated *HOOH [47,48]. The gradually increasing absorbance signals at these positions reflect the continuous accumulation of $*O_2^-$ and *HOOH on AZC-2, providing compelling evidence for the two-step $1e^-$ ORR pathway. In addition, the EPR results showed that a significant $\cdot O_2^-$ signal could be detected after 5 min of light exposure compared to the dark environment (Fig. 5c). These findings suggest that AZC-2 produces H_2O_2 by stepwise proton coupling via the two-step $1e^-$ ORR. Based on the theoretical calculations, the work functions (Φ) of ZIS, Ag-ZIS, and TpBpy COF are 4.35 eV, 4.06 eV, and 4.48 eV, respectively (Fig. 5d-f). Therefore, the E_F of Ag-ZIS is higher than those of ZIS and TpBpy COF. Fig. 5g shows a schematic of the band structure and S-scheme heterojunction. For the composite formed by COF and ZIS, a type I heterojunction is observed, where both electrons and holes prefer to migrate toward the COF, facilitating carrier recombination. Notably, the composite of Ag-ZIS and TpBpy COF forms an energy level staggered heterojunction, enabling spatial separation of electrons and holes and enhancing electron participation in the ORR reaction. Therefore, the introduction of Ag ions modulates the band structure of ZIS, shifting it upward to create a staggered type with the COF bands, highlighting the crucial positive effect of the introduction of Ag ions in this photocatalytic system. Based on the experimental results and theoretical calculations, we establish the S-scheme photocatalytic mechanism of the AZC composite.

When they are in contact in the dark, the energy band of AZ bends upward and that of COF bends downward because the Fermi energy level of AZ is higher than that of COF. Electrons of AZ are transferred to

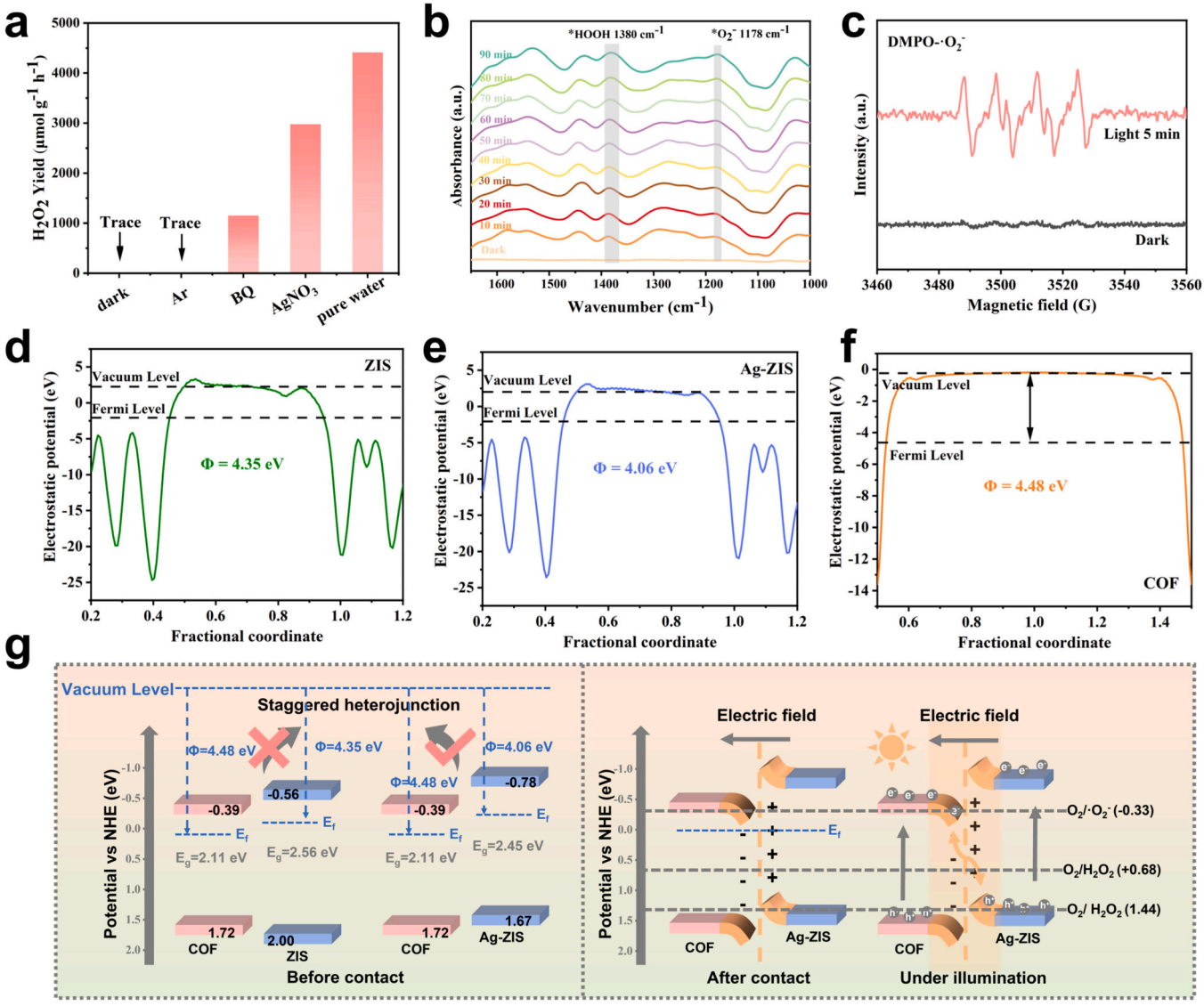

Fig. 5. (a) The influence of various conditions and different scavengers on the H_2O_2 production performance over AZC-2. (b) In-situ FTIR spectrum of AZC-2 for photocatalytic H_2O_2 production (Line of dark is under He atmosphere). (c) EPR spectra of DMPO−·O_2^- over AZC-2 at 0 min and 5 min. Calculated electrostatic potentials of (d) ZIS, (e) Ag-ZIS, and (f) AZC. (g) Schematic comparison of ZC and AZC heterojunctions and S-scheme heterojunction photocatalytic mechanism of AZC.

COF to achieve the Fermi energy level equilibrium, which results in the formation of an internal electric field (IEF) pointing from AZ to COF at their interface. Upon light excitation, photogenerated electrons in the conduction band (CB) of COF tend to transfer to the valence band (VB) of AZ and recombine with holes, consistent with the charge transfer pathways in S-scheme heterojunctions. This spatial charge separation reduces recombination and benefits photocatalysis. Moreover, the accumulated electrons in the CB of Ag-ZIS and the holes in the VB of COF exhibit significant reduction and oxidation potentials, respectively. These potentials are sufficient to drive the conversion of O_2 to $\cdot O_2^-$ (−0.33 V vs NHE) and $\cdot O_2^-$ to H_2O_2 (+1.44 V vs NHE), thereby efficiently facilitating the two-step $1e^-$ ORR pathway for H_2O_2 production.

The optimized structural models of ZIS, Ag-ZIS, and TpBpy COF are illustrated in Fig. 6a. The charge density difference distribution at the interface of AZC composites was evaluated as shown in Fig. 6b. The charge density difference distribution at AZC interfaces indicates electron migration from Ag-ZIS to TpBpy COF, demonstrating the formation of an IEF between Ag-ZIS and TpBpy COF, in agreement with the XPS results. Fig. 6c and Fig. 6d present the calculated energy profiles for O_2 reduction to H_2O_2 on AZC. The heterovalent doping of Ag creates a local charge imbalance, and this defect structure acts as an active site, which is highly favorable for the adsorption and activation of O_2. Therefore, we chose Ag site to calculate the free energy of ORR. The reduction steps from O_2 to O_2* and from OOH* to HOOH* are exothermic, indicating that these processes can proceed spontaneously without energy input. Conversely, the steps from O_2* to OOH* and from HOOH* to H_2O_2 require energy input, which is supplied by light irradiation. This underscores the critical role of light in driving this photocatalytic process.

4. Conclusion

In summary, we have successfully designed a novel Ag-doped ZIS/TpBpy COF S-scheme heterojunction through a facile room-temperature cation exchange method followed by hydrothermal synthesis, achieving efficient H_2O_2 production in the pure water system. Firstly, our system achieved a photocatalytic H_2O_2 production rate of 4425 μmol·g^{-1}·h^{-1}, surpassing recent COF-based and ZIS-based composites and demonstrating its green synthesis advantages. Crucially, we propose an

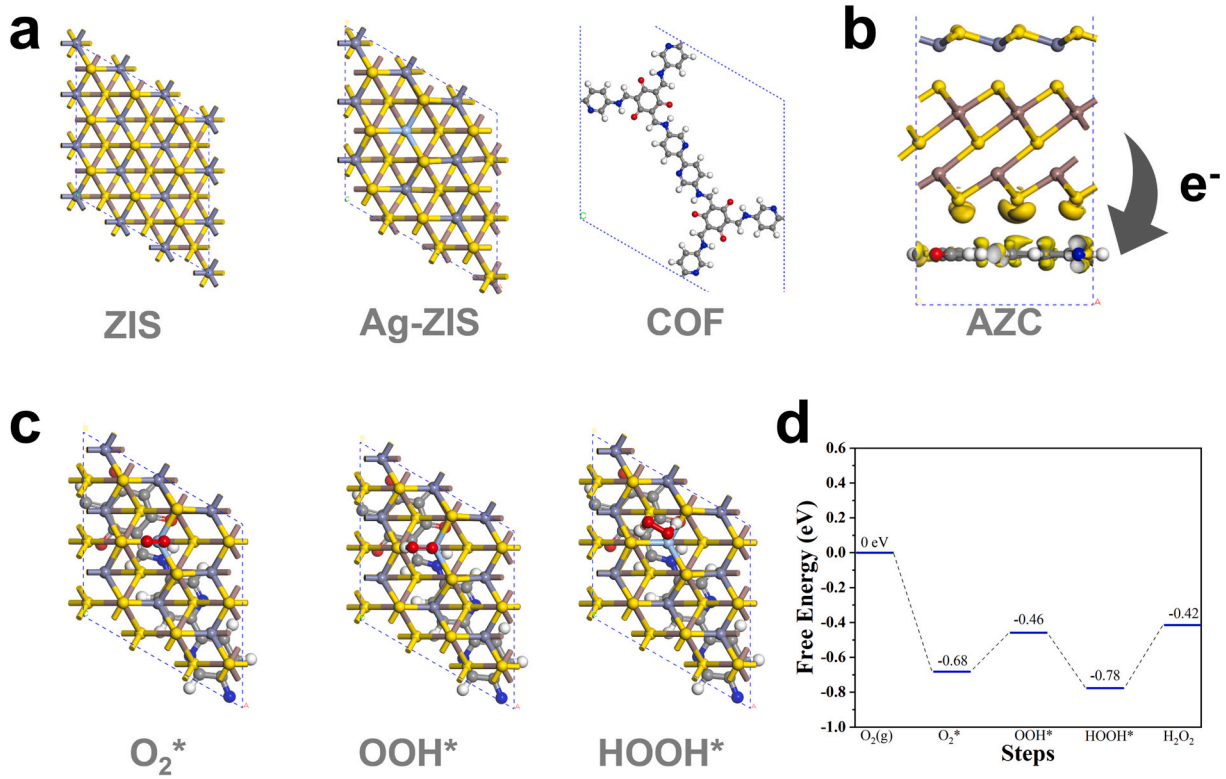

Fig. 6. (a) Structural optimization diagrams of ZIS, Ag-ZIS, and TpBpy COF. (b) Calculated 3D charge density difference distribution of AZC. (c, d) Free energy diagrams of ORR at the active sites of AZC.

innovative strategy—Ag-doping modulates the IEF in the S-scheme heterojunction. Compared to simple physical heterostructures [33,49], this strategy further accelerates charge-carrier migration, offering a new paradigm for designing high-performance photocatalysts. Furthermore, the preparation method only employs simple room-temperature cation exchange and hydrothermal methods, without any other cumbersome procedures, which enhances the material's feasibility for practical applications. Detailed characterization and experimental results indicate that the Ag ion doping modulates the electronic and band structure of ZIS, promoting the formation of an S-scheme heterojunction with TpBpy COF and enhancing electron separation and transfer. In addition, DFT calculations showed that strong interfacial interactions between Ag-ZIS and TpBpy COF promoted efficient electron transfer. Ag-doping modulates the built-in electric field in S-scheme heterojunction of $ZnIn_2S_4$/COF for efficient photocatalytic H_2O_2 production from pure water. This study innovatively proposes a synergistic hypothesis combining ion doping with S-scheme heterostructure construction, achieving a significant enhancement in photocatalytic H_2O_2 synthesis activity by regulating the electronic structure of the material and the charge transport mechanism at the interface. By pursuing a dual-path approach combining atomic-scale band structure modulation and interface charge dynamics optimization, the study addresses the common challenges of charge recombination and insufficient active sites in photocatalytic reactions. This work provides new insights into the use of MS/COF catalysts for photocatalytic H_2O_2 production and lays a theoretical foundation for the development of green and sustainable H_2O_2 production technologies. Based on this work, we will broaden this design concept to other types of MS (e.g., CdS, NiS)/COF (e.g., Pyrene-based COF, anthraquinone-based COF) photocatalysts to enhance applicability and universality. To bridge the lab-to-industry gap, we aim to develop continuously operated flow reactors for long-term performance and evaluate their functionality in complex media such as seawater or lake water, addressing practical challenges in catalyst stability and economic viability.

CRediT authorship contribution statement

Jiayi Meng: Writing – original draft, Validation, Methodology, Investigation, Conceptualization. **Yamei Huang:** Formal analysis. **Yifan Liao:** Writing – review & editing. **Quanmei Zhou:** Validation. **Yuchen Wei:** Formal analysis. **Xinglin Wang:** Investigation. **Linlin Gao:** Data curation. **Wei-Lin Dai:** Writing – review & editing, Visualization, Supervision, Project administration, Funding acquisition.

Declaration of competing interest

The authors declare that they have no known competing financial interests or personal relationships that could have appeared to influence the work reported in this paper.

Acknowledgments

This work was funded by the National Key Research and Development Program of China (2021YFA1501404), Natural Science Foundation of Shanghai (22ZR1404200), and the Science and Technology Commission of Shanghai Municipality (2024ZDSYS02).

Appendix A. Supplementary data

Supplementary data to this article can be found online at https://doi.org/10.1016/j.jcis.2025.138603.

Data availability

Data will be made available on request.

References

[1] S.P. Teong, X. Li, Y. Zhang, Hydrogen peroxide as an oxidant in biomass-to-chemical processes of industrial interest, Green Chem. 21 (2019) 5753–5780.
[2] S. Fukuzumi, Y.-M. Lee, W. Nam, Recent progress in production and usage of hydrogen peroxide, Chin. J. Catal. 42 (2021) 1241–1252.
[3] Z. Chen, D. Yao, C. Chu, S. Mao, Photocatalytic H_2O_2 production systems: design strategies and environmental applications, Chem. Eng. J. 451 (2023) 138489.
[4] J. García-Serna, T. Moreno, P. Biasi, M.J. Cocero, J.-P. Mikkola, T.O. Salmi, Engineering in direct synthesis of hydrogen peroxide: targets, reactors and guidelines for operational conditions, Green Chem. 16 (2014) 2320–2343.
[5] S.C. Perry, D. Pangotra, L. Vieira, L.-I. Csepei, V. Sieber, L. Wang, C. Ponce de León, F.C. Walsh, Electrochemical synthesis of hydrogen peroxide from water and oxygen, Nat. Rev. Chem. 3 (2019) 442–458.
[6] G. Gao, Y. Tian, X. Gong, Z. Pan, K. Yang, B. Zong, Advances in the production technology of hydrogen peroxide, Chin. J. Catal. 41 (2020) 1039–1047.
[7] H. Hou, X. Zeng, X. Zhang, Production of hydrogen peroxide by photocatalytic processes, Angew. Chem. Int. Ed. 59 (2020) 17356–17376.
[8] T. Freese, J.T. Meijer, B.L. Feringa, S.B. Beil, An organic perspective on photocatalytic production of hydrogen peroxide, Nat. Catal. 6 (2023) 553–558.
[9] D. Tan, R. Zhuang, R. Chen, M. Ban, W. Feng, F. Xu, X. Chen, Q. Wang, Covalent organic frameworks enable sustainable solar to hydrogen peroxide, Adv. Funct. Mater. 34 (2024) 2311655.
[10] M. Li, Q. Zheng, D.P. Durkin, H. Chen, D. Shuai, Environmental application of chlorine-doped graphitic carbon nitride: continuous solar-driven photocatalytic production of hydrogen peroxide, J. Hazard. Mater. 436 (2022) 129251.
[11] H. Qin, L. Sun, S. Zou, A. Bian, Y. Cui, J. Hou, C. Lu, C. Li, F. Guo, W. Shi, Boosted photocatalytic H_2O_2 production in pure water with amino-modified N, S-doped carbon dots, Chem. Eng. J. 499 (2024) 156239.
[12] X. Lu, Z. Chen, Z. Hu, F. Liu, Z. Zuo, Z. Gao, H. Zhang, Y. Zhu, R. Liu, Y. Yin, Y. Cai, D. Ma, Q. Zhang, Boosted charge transfer for highly efficient photosynthesis of H_2O_2 over Z-scheme I^-/K^+ co-doped g-C_3N_4/metal–organic-frameworks in pure water under visible light, Adv. Energy Mater. 14 (2024) 2401873.
[13] C. Yu, J. He, M. Tan, Y. Hou, H. Zeng, C. Liu, H. Meng, Y. Su, L. Qiao, T. Lookman, Y. Bai, Selective enhancement of photo-piezocatalytic performance in $BaTiO_3$ via heterovalent ion doping, Adv. Funct. Mater. 32 (2023) 2209365.
[14] B. Zhu, J. Sun, Y. Zhao, L. Zhang, J. Yu, Construction of 2D S-scheme heterojunction photocatalyst, Adv. Mater. 36 (2024) 2310600.
[15] H. Liu, M. Yan, Z. Wang, G. Xie, X. Pu, Y. Fu, X. Peng, H. Wang, J. Wang, Constructing boosted charge separation for efficient H_2O_2 production and pollutant degradation by highly defective $ZnIn_2S_4$/ carbon doped boron nitride, J. Environ. Chem. Eng. 12 (2024) 114251.
[16] E.S. Ghalehsefid, Z.G. Jahani, A. Aliabadi, M. Ghodrati, A. Khamesan, A. Parsaei-Khomami, M. Mousavi, M.-A. Hosseini, J.B. Ghasemi, X. Li, TiO_2 nanotube/$ZnIn_2S_4$ nanoflower composite with step-scheme heterojunction for efficient photocatalytic H_2O_2 production and organic dye degradation, J. Environ. Chem. Eng. 11 (2023) 110160.
[17] X. Zeng, Y. Liu, Y. Kang, Q. Li, Y. Xia, Y. Zhu, H. Hou, M. Uddin, T. Gengenbach, D. Xia, C. Sun, D. McCarthy, A. Deletic, J. Yu, X. Zhang, Simultaneously tuning charge separation and oxygen reduction pathway on graphitic carbon nitride by polyethylenimine for boosted photocatalytic hydrogen peroxide production, ACS Catal. 10 (2020) 3697–3706.
[18] Y. Huang, H. Gu, H. Zhang, X. Wang, L. Gao, Y. Cui, B. Zong, H. Li, W.-L. Dai, Synergistic V–Nb sites modulate selective alkene epoxidation with in situ photogenerated H_2O_2 over COF@MXene heterostructures, ACS Catal. 14 (2024) 12541–12550.
[19] L. Zhang, J. Zhang, H. Yu, J. Yu, Emerging S-scheme photocatalyst, Adv. Mater. 34 (2022) 2107668.
[20] K. Meng, J. Zhang, B. Cheng, X. Ren, Z. Xia, F. Xu, L. Zhang, J. Yu, Plasmonic near-infrared-response S-scheme ZnO/$CuInS_2$ photocatalyst for H_2O_2 production coupled with glycerin oxidation, Adv. Mater. 36 (2024) 2406460.
[21] Y. Yang, B. Cheng, J. Yu, L. Wang, W. Ho, TiO_2/In_2S_3 S-scheme photocatalyst with enhanced H_2O_2-production activity, Nano Res 16 (2021) 4506–4514.
[22] X. Ma, S. Li, Y. Gao, N. Li, Y. Han, H. Pan, Y. Bian, J. Jiang, S-scheme heterojunction fabricated from covalent organic framework and quantum dot for enhanced photosynthesis of hydrogen peroxide from water and air, Adv. Funct. Mater. 34 (2024) 2409913.
[23] H. Zhang, Y. Huang, X. Wang, J. Meng, L. Gao, Y. Li, Y. Zhang, Y. Liao, W.-L. Dai, Tightly-bound interfaces between $ZnIn_2S_4$ nanosheets and few-layered Mo_2TiC_2 MXene induced highly efficient noble-metal-free Schottky junction for photocatalytic hydrogen evolution, Sep. Purif. Technol. 360 (2025) 131199.
[24] Y. Li, Y. Huang, H. Zhang, X. Wang, L. Gao, Y. Zhang, Y. Liao, J. Meng, Y. Cui, W.-L. Dai, In-situ construction of 3D/2D $ZnIn_2S_4$/Ni-MOLs: highly efficient visible-light-driven photocatalytic heterojunction in hydrogen evolution, Appl. Catal. B-Environ. 361 (2025) 124657.
[25] H. Peng, H. Yang, J. Han, X. Liu, D. Su, T. Yang, S. Liu, C.-W. Pao, Z. Hu, Q. Zhang, Y. Xu, H. Geng, X. Huang, Defective $ZnIn_2S_4$ nanosheets for visible-light and sacrificial-agent-free H_2O_2 photosynthesis via O_2/H_2O redox, J. Am. Chem. Soc. 145 (2023) 27757–27766.
[26] J. Wan, Y. Wang, J. Liu, R. Song, L. Liu, Y. Li, J. Li, J. Low, F. Fu, Y. Xiong, Full-space electric field in Mo-decorated $Zn_2In_2S_5$ polarization photocatalyst for oriented charge flow and efficient hydrogen production, Adv. Mater. 36 (2024) 2405060.
[27] M. Yang, X.-Q. Zhan, D.-L. Ou, L. Wang, L.-L. Zhao, H.-L. Yang, Z.-Y. Liao, W.-Y. Yang, G.-Z. Ma, H.-L. Hou, Efficient visible-light-driven hydrogen production with ag-doped flower-like $ZnIn_2S_4$ microspheres, Rare Metals 44 (2024) 1024–1041.
[28] A.P. Côté, A.I. Benin, N.W. Ockwig, M. O'Keeffe, A.J. Matzger, O.M. Yaghi, Porous, crystalline, covalent organic frameworks, Science 310 (2005) 1166–1170.
[29] C. Wang, Z. Zhang, Y. Zhu, C. Yang, J. Wu, W. Hu, 2D covalent organic frameworks: from synthetic strategies to advanced optical-electrical-magnetic functionalities, Adv. Mater. 34 (2022) 2102290.
[30] J. Zhang, F. Xue, Z. Wang, Terpyridine- and quarterpyridine-based cationic covalent organic frameworks for visible-light-catalytic H_2O_2 synthesis, Angew. Chem. Int. Ed. e202425617 (2025).
[31] C. Krishnaraj, H. Jena, L. Bourda, A. Laemont, P. Pachfule, J. Roeser, C. V. Chandran, S. Borgmans, S.M.J. Rogge, K. Leus, C.V. Stevens, J.A. Martens, V. Van Speybroeck, E. Breynaert, A. Thomas, P. Van Der Voort, Strongly reducing (diarylamino)benzene-based covalent organic framework for metal-free visible light photocatalytic H_2O_2 generation, J. Am. Chem. Soc. 142 (2020) 20107–20116.
[32] J. Hao, Y. Tang, J. Qu, Y. Cai, X. Yang, J. Hu, Robust covalent organic frameworks for photosynthesis of H_2O_2: advancements, challenges and strategies, Small 20 (2024) 2404139.
[33] H. Chen, S. Gao, G. Huang, Q. Chen, Y. Gao, J. Bi, Built-in electric field mediated S-scheme charge migration in COF/In_2S_3 heterojunction for boosting H_2O_2 photosynthesis and sterilization, Appl. Catal. B-Environ. 343 (2024) 123545.
[34] Y. Zhang, Y. Huang, X. Wang, H. Zhang, L. Gao, Y. Li, Y. Liao, J. Meng, Y. Cui, Z. Li, W.-L. Dai, Interface interaction modulates charge transfer in flower-like In_2S_3 nanosheets/COF composite for efficient solar-to-H_2O_2 conversion, Sep. Purif. Technol. 358 (2024) 130374.
[35] Y. Feng, J. Li, S. Ye, S. Gao, R. Cao, Growing COFs in situ on CdS nanorods as core-shell heterojunctions to improve the charge separation efficiency, Sustainable Energy Fuels 6 (2022) 5089.
[36] Q. Shang, Y. Liu, J. Ai, Y. Yan, X. Yang, D. Wang, G. Liao, Embedding au nanoclusters into the pores of carboxylated COF for the efficient photocatalytic production of hydrogen peroxide, J Mater Chem A 11 (2023) 21109–21122.
[37] Y. Zhang, Z. Hu, H. Zhang, H. Li, S. Yang, Uncovering original Z scheme heterojunctions of COF/MO_x (M = Ti, Zn, Zr, Sn, Ce, and Nb) with ascendant photocatalytic selectivity for virtually 99.9% NO-to-NO_3^- oxidation, Adv. Funct. Mater. 33 (2023) 2303851.
[38] Q. Guan, L.-L. Zhou, Y.-B. Dong, Construction of covalent organic frameworks via multicomponent reactions, J. Am. Chem. Soc. 145 (2023) 1475–1496.
[39] Y. Zhang, J. Qiu, B. Zhu, M.V. Fedin, B. Cheng, J. Yu, L. Zhang, ZnO/COF S-scheme heterojunction for improved photocatalytic H_2O_2 production performance, Chem. Eng. J. 444 (2022) 136584.
[40] J. Sun, H. Sekhar Jena, C. Krishnaraj, K. Singh Rawat, S. Abednatanzi, J. Chakraborty, A. Laemont, W. Liu, H. Chen, Y.-Y. Liu, K. Leus, H. Vrielinck, V. Van Speybroeck, P. Van Der Voort, Pyrene-based covalent organic frameworks for photocatalytic hydrogen peroxide production, Angew. Chem. Int. Ed. 62 (2023) e202216719.
[41] A. Chakraborty, A. Alam, U. Pal, A. Sinha, S. Das, T. Saha-Dasgupta, P. Pachfule, Enhancing photocatalytic hydrogen peroxide generation by tuning hydrazone linkage density in covalent organic frameworks, Nat. Commun. 16 (2025) 503.
[42] Y.X. Liu, L. Li, H. Tan, N. Ye, Y. Gu, S.Q. Zhao, S.P. Zhang, M.C. Luo, S.J. Guo, Fluorination of covalent organic framework reinforcing the confinement of Pd nanoclusters enhances hydrogen peroxide photosynthesis, J. Am. Chem. Soc. 145 (2023) 19877–19884.
[43] F. Liu, P. Zhou, Y. Hou, H. Tan, Y. Liang, J. Liang, Q. Zhang, S. Guo, M. Tong, J. Ni, Covalent organic frameworks for direct photosynthesis of hydrogen peroxide from water, air and sunlight, Nat. Commun. 14 (2023) 4344.
[44] J.-Y. Yue, L.-P. Song, Y.-F. Fan, Z.-X. Pan, P. Yang, Y. Ma, Q. Xu, B. Tang, Thiophene-containing covalent organic frameworks for overall photocatalytic H_2O_2 synthesis in water and seawater, Angew. Chem. Int. Ed. 62 (2023) e202309624.
[45] T. Kim, D.-Y. Lee, E. Choi, H.-I. Kim, B.-S. Kim, Simultaneous photocatalytic hydrogen peroxide production and pollutant degradation via bipyridine-based polyimide covalent organic framework, Appl. Catal. B-Environ. 357 (2024) 124264.
[46] K. Wang, J. Li, X. Liu, Q. Cheng, Y. Du, D. Li, G. Wang, B. Liu, Sacrificial-agent-free artificial photosynthesis of hydrogen peroxide over step-scheme WO_3/NiS hybrid nanofibers, Appl. Catal. B-Environ. 342 (2024) 123349.
[47] P. Liu, T. Liang, Y. Li, Z. Zhang, Z. Li, J. Bian, L. Jing, Photocatalytic H_2O_2 production over boron-doped g-C_3N_4 containing coordinatively unsaturated FeOOH sites and CoO_x clusters, Nat. Commun. 15 (2024) 9224.
[48] L. Zhang, C. Wang, Q. Jiang, P. Lyu, Y. Xu, Structurally locked high-crystalline covalent triazine frameworks enable remarkable overall photosynthesis of hydrogen peroxide, J. Am. Chem. Soc. 146 (2024) 29943–29954.
[49] H. Zhang, J. Liu, Y. Zhang, B. Cheng, B. Zhu, L. Wang, BiOBr/COF S-scheme photocatalyst for H_2O_2 production via concerted two-electron pathway, J. Mater. Sci. Technol. 166 (2023) 241–249.